In operando study of gypsum crystal growth through in-cell environmental SEM

Alexandre Fantou, Annie Malchère, Anna Wozniak, Lucian Roiban, Sylvain Meille, Karine Masenelli-Varlot, Solène Tadier

Graphical Abstract

In operando study of gypsum crystal growth through in-cell environmental SEM

Alexandre Fantou, Annie Malchère, Anna Wozniak, Lucian Roiban, Sylvain Meille, Karine Masenelli-Varlot, Solène Tadier

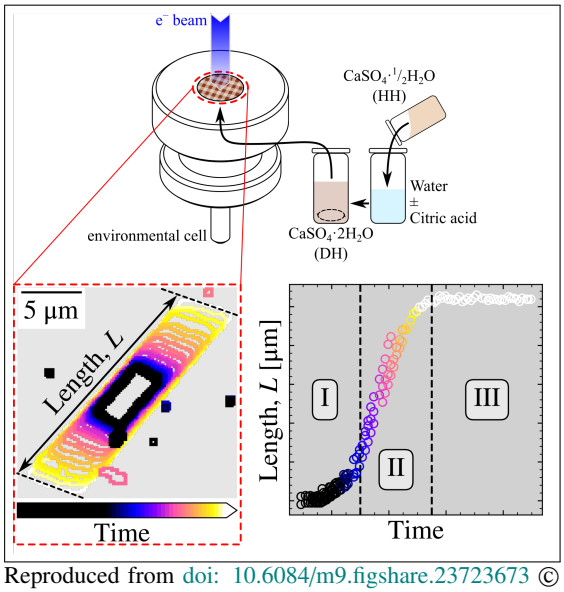

Highlights

In operando study of gypsum crystal growth through in-cell environmental SEM

Alexandre Fantou, Annie Malchère, Anna Wozniak, Lucian Roiban, Sylvain Meille, Karine Masenelli-Varlot, Solène Tadier

- Evolution of gypsum plaster was analyzed during setting in conditions of use in SEM
- Kinetics of the growth of >100 gypsum crystals was computed from image analysis
- Growth rates of the gypsum facets were computed from crystallographic indexation
- A same gypsum crystal may experience different growth regimes along time
- A slower growth is experienced by crystals with thermodynamically unstable facets

In operando study of gypsum crystal growth through in-cell environmental SEM

Alexandre Fantou[a], Annie Malchère[a], Anna Wozniak[a], Lucian Roiban[a], Sylvain Meille[a], Karine Masenelli-Varlot[a], Solène Tadier[a,*]

[a]*Univ Lyon, INSA Lyon, Université Claude Bernard Lyon 1, CNRS, MATEIS, UMR5510, Villeurbanne, 69621, France*

Abstract

Thanks to their setting ability, hydraulic binder materials (*e.g.*, cements, plasters) are used for a wide variety of applications (*e.g.*, construction, medical). The setting reaction occurs through a dissolution – precipitation mechanism during which initial particles dissolve releasing ionic species from which new crystals precipitate. The development of such a microstructure governs the final properties of the material and are thus of uttermost interest.

In this paper, the *in operando* study of the precipitation of gypsum crystals from the dissolution of bassanite particles using a specific cell for SEM observation is presented. Image analysis based on segmentation enabled to give quantitative results on the growth of crystals at global and local scales. Single crystal facets are indexed based on crystallography and literature results, which enables the quantification of crystal growth rates for the indexed crystallographic planes.

Keywords: Setting reaction, β– calcium sulfate, Microstructure, Image analysis, Crystallography, *in situ*

1. Introduction

Hydraulic binders (cements, gypsum plaster) are processed through dissolution-precipitation. While calcium sulfates are widely used in the form of gypsum boards for interior partitions, they are also often used as model materials for crystallization studies. This is explained by a relatively simple chemical reaction involving only crystalline phases, from common and cheap materials, with relatively large crystal sizes (microns to tens/hundreds of microns, possibly several meters in exceptional cases).

The processing of calcium sulfates starts with the dissolution of calcium sulfate hemihydrate (HH), also known as bassanite or plaster, followed by the precipitation of calcium sulfate dihydrate crystals (DH), also known as gypsum. The reaction usually takes place within minutes, with a complete hydration being reached in a maximum of one hour if no retardants are used. The hydration reaction is given here in eq. (1):

$$CaSO_4 \cdot \frac{1}{2}H_2O + \frac{3}{2}H_2O \longrightarrow CaSO_4 \cdot 2H_2O + Q \quad (1)$$

with Q the heat of reaction arising from the dissolution of calcium sulfate hemihydrate.

Historically, optical microscopy (OM) was first used to follow the growth of gypsum crystals, from supersaturated solutions in highly dilute systems [1, 2]. In the absence of additives, observed DH crystals were generally needle- and plate-like with wide size distributions. This method, although limited in terms of spatial resolution, enabled the quantification of various aspects of the precipitation of dihydrate crystals

*Corresponding author: solene.tadier@insa-lyon.fr

(*e.g.*, evolutions of shape and dimensions of crystals, effects of additives on crystallization, linear growth rates, kinetic order of the reaction rate). Combined with chemical analysis of the solution, it also provided information for measuring the induction period of the precipitation of DH crystals, during which nuclei are formed and start to grow by a "slow" process to form small crystallites [1].

To reach higher spatial resolutions, the evolution of the microstructure of calcium sulfate samples was studied with Scanning Electron Microscopy (SEM). To observe samples representative of industrial applications, *i.e.*, with typical liquid-to-solid mass (L/S) ratios below 1, the setting reaction was stopped by soaking and grinding samples into ethanol [3]; samples could then be studied once dried. The growth of gypsum crystals around HH particles followed by their entanglement at later stages were both evidenced, but no image analysis was performed for the quantification of the reaction extent. The need to stop the setting reaction (destructive characterization) impeded to follow the *in operando* evolution of one specific sample. Morever, the preparation protocol may have affected the composition and morphology of the studied samples, as quenching crystallizing plaster in ethanol may stabilize HH with respect to DH, or even promote the formation of HH from already grown DH crystals, rather than preserving them [4, 5]. To solve this issue, the setting of gypsum paste was also monitored using a cell specifically designed for SEM observation, closed by a polymer membrane that is transparent to the electron beam, but water and air tight, protecting the setting paste from the chamber conditions (*e.g.*, vacuum) [6]. Thus, samples could be studied while they set, and with L/S ratios typical of industrial applications. In [6], the growth of needle-like gypsum crystals followed by their entanglement was regularly monitored within the first hour of reaction (after a dead-time of 17 min), while the growth of crystals was not completed yet. The study lacked from quantitative data describing the evolution of gypsum growth during setting reaction. Moreover, the influence of both the electron beam and the membrane on the development of the microstructure were still pending.

To study the early stages of gypsum nucleation, Transmission Electron Microscopy (TEM) was used either in High Resolution mode (HR TEM) after quenching of undersatured solution [7], in cryogenic mode, or using a liquid cell to enable real time follow-up of the reaction [8]. In this latter work carried out in solution rather than in concentrated pastes, DH crystals were shown to nucleate on dissolving HH rod-shaped particles [8]. Still at the nanoscale, the motions of crystalline steps at the surface of DH crystals were investigated using Atomic Force Microscopy (AFM) [9–15]. However, this technique can neither be used for the characterization of setting pastes with representative L/S ratios, nor for the simultaneous monitoring of the dissolution of HH particles and the precipitation of DH crystals at a more global scale.

In situ monitoring of the setting reaction from dissolution of HH was also followed up at the mesoscale using X-ray tomography (µ-CT) [16, 17] and by combining 3D X-ray diffraction (s3DXRD) with phase contrast tomography (PCT) [18]. Advantages of these techniques are their non-destructive nature, the ease of sample preparation with no requirements in terms of paste fluidity or L/S ratio and 3D data providing information on the bulk of a sample. In all cases, the dissolution of HH grains, the formation of a porous network and the non-epitaxial growth of needle and plate-shaped interlocked DH crystals led to complex microstructures. With µ-CT (typical voxel sizes of 2.5 µm and of 0.65 µm to 0.163 µm, using laboratory and synchrotron X-ray tomographies, respectively), a "microstructural degree of reaction" was computed from the mean evolutions of volume fractions of dissolving HH particles and of precipitating DH crystals. At the single-grain scale, size measurements of individual HH and of DH crystals enabled to determine average dissolution and precipitation rates during setting reaction [16, 17]. The combination of s3DXRD with PCT enabled to identify reacting planes of the HH crystals and to monitor their evolution during dissolution. It was thus shown that the (100) and (010) planes of HH grains were preferentially dissolved [18]. However, nucleation of DH crystals could not be observed at this scale due to resolution limit, and observing their growth was particularly difficult during the early stages of the reaction [16–18].

In this paper, the same type of environmental cell as in [6] is used to monitor the precipitation of DH crystals from the dissolution of calcium sulfate HH particles *in operando*, until the microstructure seems not to evolve anymore. Then, image analysis of micrographs collected every minute enables to quantify the growth of DH crystals both at a global and at a local scale. The identification of growth directions and faces of DH crystals is also performed, enabling the measurement of the growth rates for each type of crystal planes along the reaction and in conditions of use (*e.g.*, L/S ratio, ...)

2. Materials and Methods

2.1. Gypsum plaster

Gypsum plaster ($CaSO_4 \cdot 2H_2O$) was obtained by mixing a HH powder ($\beta - CaSO_4 \cdot \frac{1}{2}H_2O$) with an aqueous solution. The liquid to solid mass ratio (L/S) was set to 0.6. The time at which the powder and the solution got in contact was defined as t_0 and corresponds to the origin of times for all experiments ($t_0 = 0$).

The calcium sulfate reactive powder was an industrial product from Mátra factory (Rigips, Halmajugra, Hungary). It was mostly composed of calcium sulfate hemihydrate (bassanite, $\beta - CaSO_4 \cdot \frac{1}{2}H_2O$) around 90 $_{wt}\%$ and in lower extents of anhydrous calcium sulfate (anhydrite, $CaSO_4$), calcium carbonate (calcite, $CaCO_3$), silicon dioxide (quartz, SiO_2) and aluminosilicates.

Citric acid monohydrate $C_6H_8O_7 \cdot H_2O$ (EMSURE Merck KGaA, Darmstadt, Germany, Catalog # 1002441000, Batch # K50959644) was used as a retardant of the hydration reaction. Two solutions were used, one consisting of pure deionized water (resistivity of 18 $M\Omega \cdot cm$) and the other one consisting of a 5.2 mM citric acid solution prepared with deionized water.

2.2. In situ SEM

Encapsulating cells QX202C from El-Mul (QuantomiX Ltd, Rehovot, Israel) were used to study the setting reaction of calcium sulfate hemihydrate with SEM under standard conditions (*i.e.*, atmospheric pressure, humidity). A scheme of the QX202C cell is illustrated in fig. 1(a). This cell, of inner volume comprised between 6.5 µL and 7.5 µL, is closed by a top membrane, which is electron transparent but air- and water- tight. Thus, the wet setting paste, introduced inside the cell before its closure, is isolated from the vacuum of the SEM chamber.

Plaster paste was prepared by sprinkling 5 g of the HH powder in 3 g of the solution during 30 s. The obtained mixture was then manually mixed during another 30 s using a spatula describing movements in a figure of eight. Following the instructions of the QX202C cell furnisher, two volumes of 3.5 µL of the plaster paste were collected and deposited in the open encapsulating cell by means of a micropipette Microman M25 (Gilson, Middleton, Wisconsin, USA). Then, the cell was closed, and placed in the SEM chamber to start the observation as soon as possible, once the vacuum was ready.

The observation area was chosen by scanning the top of the cell (*i.e.*, grid, see fig. 1(b)) to check the homogeneity of the sample. Note the presence of the metallic grid, helpful to spatially locate different interesting spots.

The scanning electron microscope used is a ZEISS Supra 55VP SEM (Carl Zeiss Microscopy GmbH, Oberkochen, Germany) equipped with a Field Emission Gun. The acceleration voltage was set to 10 kV and the cell in which was introduced the setting paste was placed at a working distance of 10 mm. Images were acquired regularly using either the secondary electron Everhardt-Thornley detector, or a backscattered electron detector. The time step between two consecutive acquisitions was 30 s until a certain point where it reached 1 min when the microstructure seemed not evolve anymore. The time to record a micrography, denoted Δt_{acq}, lied between 3.8 s and 13.6 s (*cf.* table 1). Between two image acquisitions, the beam was

blanked to prevent irradiation damage in the sample. Two magnifications were used in order to image both the grid at lower magnification (pixel dimension of 744.3 nm) and the crystals at higher magnification (pixel dimension of 139.6 nm). The times of the first and last image acquisitions at higher magnification were denoted t_1 and t_{last}, respectively. t_1 corresponds to the dead-time required to get ready after mixing the HH powder with the liquid solution; it was typically of around 10 min to 15 min (*cf.* table 1). t_{last} was reached when no more significant evolution could be observed. The cell was then retrieved from the SEM chamber and stored at room temperature to make sure the setting reaction could proceed up to completion.

Some additional SEM observations were performed many days after (at t_∞, see table 1) at the very same locations with the same acquisition parameters (*i.e.*, working distance, acceleration voltage, magnification) to get information on the microstructure, once the plaster was completely set.

2.3. Image analysis

ImageJ / Fiji software was used to perform image processing and analysis [19]. All images of a same experiment (from t_1 to t_{last}) were first gathered into a stack (generating a timelapse, such as in [20]), in order to easily apply filters, and to account for the 2D microstructure evolution. First treatments on the stacks consisted of enhancing the contrast, denoising, and correcting background. Then the stacks were aligned to correct the sample drift. After a final median filtering, images were cropped in order to obtain a suitable size for observation and quantification. Typically, for the experiment illustrated in fig. 3, the final area was (130×70) µm^2 (*cf.* table 1). This area was large enough to image a sufficient number of DH crystals (at least 100 of them) and thus to give a good representation of the evolution of the setting paste microstructure.

Table 1: Summary of all the experimental conditions for *in situ* SEM acquisitions. From left to right: citric acid concentration ([CAc.] in mM), experiment number, times of the first (t_1) and last (t_{last}) images, time of the infinite image (t_∞), acquisition duration of an image (Δt_{acq}) and surface area of the region of observation. Times of the first, last and of the infinite images are given with respect to the mixing time $t_0 = 0$.

[CAc.]	Exp.	t_1	t_{last}	t_∞	Δt_{acq}	Area [µm^2]
5.2	1	29 min, 15 s	1 h, 50 min	–	3.8 s	$(133.5 \times 71.1) = 9\,483$
	2	14 min, 47 s	1 h, 17 min	6 d, 21 h	13.6 s	$(71.1 \times 46.9) = 3\,333$
	3	13 min, 45 s	1 h, 39 min	–	3.8 s	$(129.1 \times 85.9) = 11\,086$
	4	12 min, 32 s	2 h, 22 min	20 d, 22 h	13.6 s	$(125.6 \times 73.3) = 9\,208$
	5	14 min, 33 s	3 h, 58 min	–	13.6 s	$(119.2 \times 66.7) = 7\,955$
0.0	1'	13 min, 50 s	1 h, 28 min	9 d, 2 h	13.6 s	$(132.3 \times 89.3) = 11\,824$
	2'	11 min, 25 s	2 h, 53 min	–	13.6 s	$(139.3 \times 93.4) = 13\,012$

2.4. X-ray tomography

Quantitative results obtained with SEM experiments at the surface of QX202C cells were compared with 3D reconstructions of microstructures of plaster set both within and outside the cells. Computed X-ray tomography (µ-CT) was performed on an EasyTom Nano (RX Solutions, Chavanod, France) with a voltage of 100 kV and a current intensity of 145 µA. The voxel size reached for the tomographies on set plaster within and outside the cell were 2.5 µm and 0.3 µm, respectively. The latter resolution enabled to performed cross sections in the volumes to compare surface and bulk information obtained from SEM and µ-CT with resolutions of 139.6 nm and 300 nm, respectively.

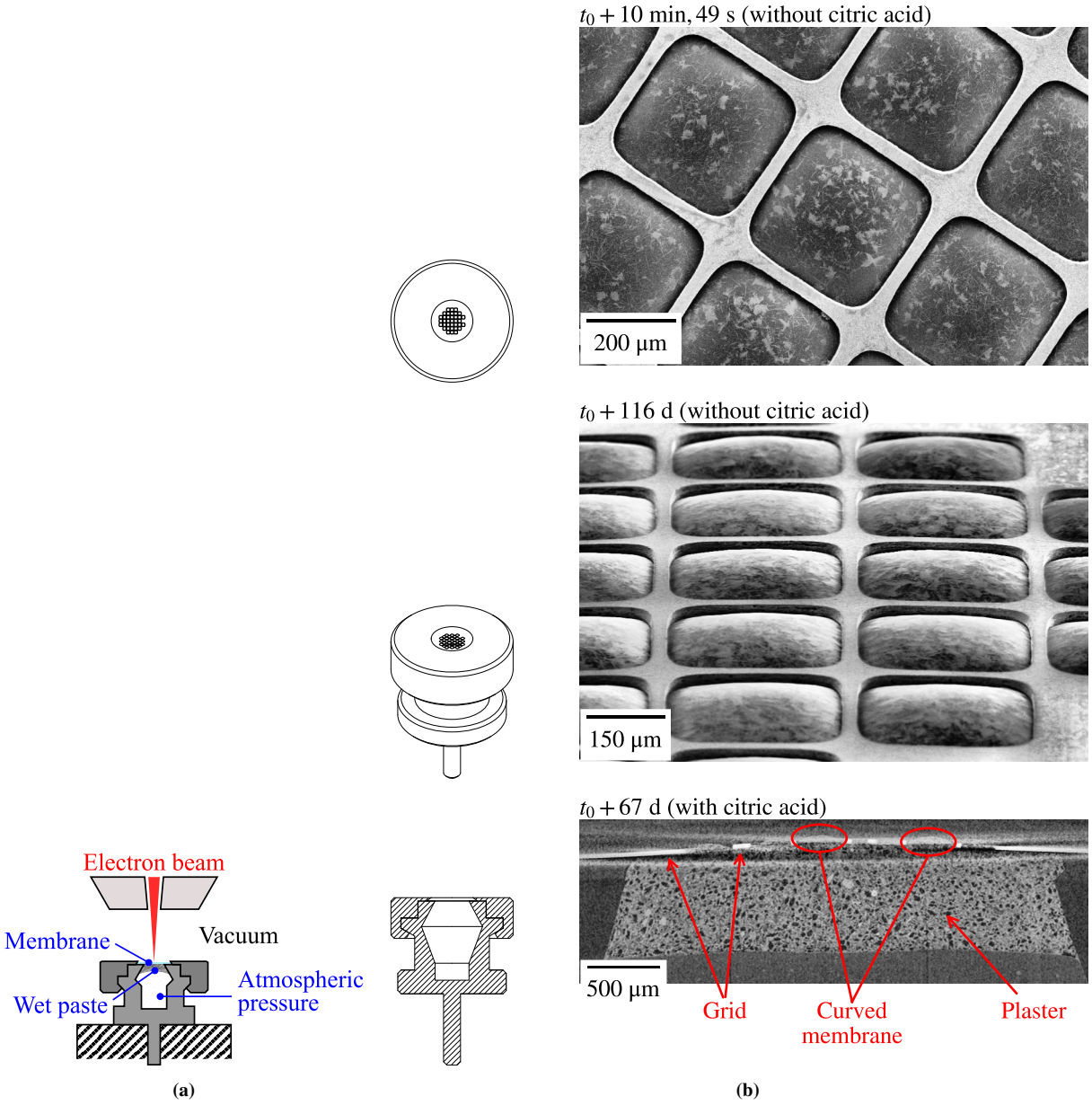

Figure 1: QuantomiX QX202C cell used to monitor DH crystals growth in liquid conditions in a SEM. **(a)** Scheme of the setup. **(b)** From top to bottom, observations of the cell with gypsum crystals: top and radial views obtained by SEM, cross section view obtained from a slice of a reconstructed volume with µ–CT (voxel size of 2.5 µm). Reproduced from doi: 10.6084/m9.figshare.23723673 © (2023) A. Fantou, CC BY 4.0 license `https://creativecommons.org/licenses/by/4.0/`.

3. Results

Figure 2 illustrates typical observations made during the setting of plaster without any retardant. In the first images, acquired around 13 min after mixing of powder and deionized water, many particles (in bright) are already observed, scattered in the liquid setting paste (in dark). The crystals present two types of morphologies: some are elongated, in the shape of thin needles of a few tens of micrometers long and

around 1 µm thick, while others form platelets, which often appear as flat and twinned crystals. The top view of the QX202C cell (fig. 2(a)) shows that the particle distribution is relatively homogeneous and similar among all windows of the grid: a focus at higher magnification can be made on a smaller zone to better describe the evolution of gypsum crystals with time (fig. 2(b)). While it seems that very few new crystals are formed after the first image (at t_1), most of them grow up to around 30 min, occupying a larger surface area than in the first image. No more significant evolution can be observed after around 30 min, and the same crystals can still be observed after a very long time ($t_\infty > 9$ days), when enough time is provided for the setting reaction to complete within the QX202C cell, kept out the microscope.

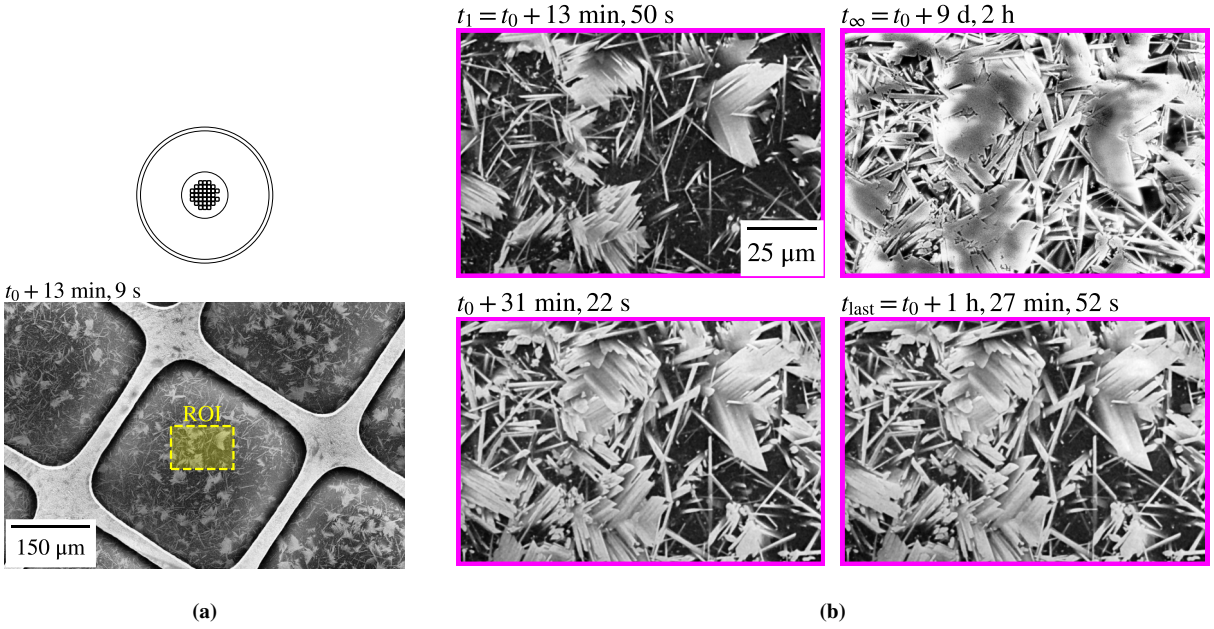

Figure 2: *In situ* micrographies of gypsum plaster crystals growing without citric acid in QX202C cell from experiment 1'. For experiment details, refer to table 1. **(a)** Overview of the grid and location of the region of interest (ROI) 13 min after t_0 and **(b)** Zoom in the ROI monitored at different times (including t_1 and t_{last}, times of first and last images, respectively, and t_∞, collected many days after at the same location). The timelaspe obtained from these micrographies can be found in [21]. Reproduced from doi: 10.6084/m9.figshare.23723673

When the plaster is prepared with the 5.2 mM citric acid solution (fig. 3), no grown crystals are seen in the first images. Observed bright points (see for instance fig. 3(b), time t_1) may correspond to small HH particles not yet dissolved, to DH seeds or due to noise artifacts from the acquisition. Then, the growth of DH seeds can be monitored all along the experiment. The crystals grow for more than 2 h (fig. 3(b)). At this point, as for fig. 2, both platelets and acicular crystals can be observed, even though it seems that fewer twinned crystals can be observed than when the plaster is prepared without citric acid (fig. 2). The top view of the grid (fig. 3(a)) gives a more complete overview of the spatial distribution of gypsum crystals at the surface of the QX202C cell, at the beginning and after crystal growth (after ca. 13 min and 2h, respectively). Although the whole surface can be depicted as relatively homogeneous, denser (*i.e.*, brighter) zones can be observed among few places, where crystals are less densely packed (*i.e.*, darker areas).

The use of citric acid as a retardant enables to monitor better the early stages of the dissolution-precipitation reaction, as shown by comparing figs. 2 and 3. Experiments conducted with citric acid permitted to observe: *(i)* the initial presence of DH seeds followed by *(ii)* growth of DH crystals with time,

whereas only the step *(ii)* could be observed in experiments conducted without citric acid.

To quantify the evolution of the extent of the setting reaction with time, image analysis was performed on all stacks of micrographies obtained for each *in operando* experiment. To do so, HH and DH particles have to be identified to follow the dissolution of HH particles on the one hand and the precipitation of DH crystals on the other hand. The methodology developed in this work, based on segmentation of the imaged

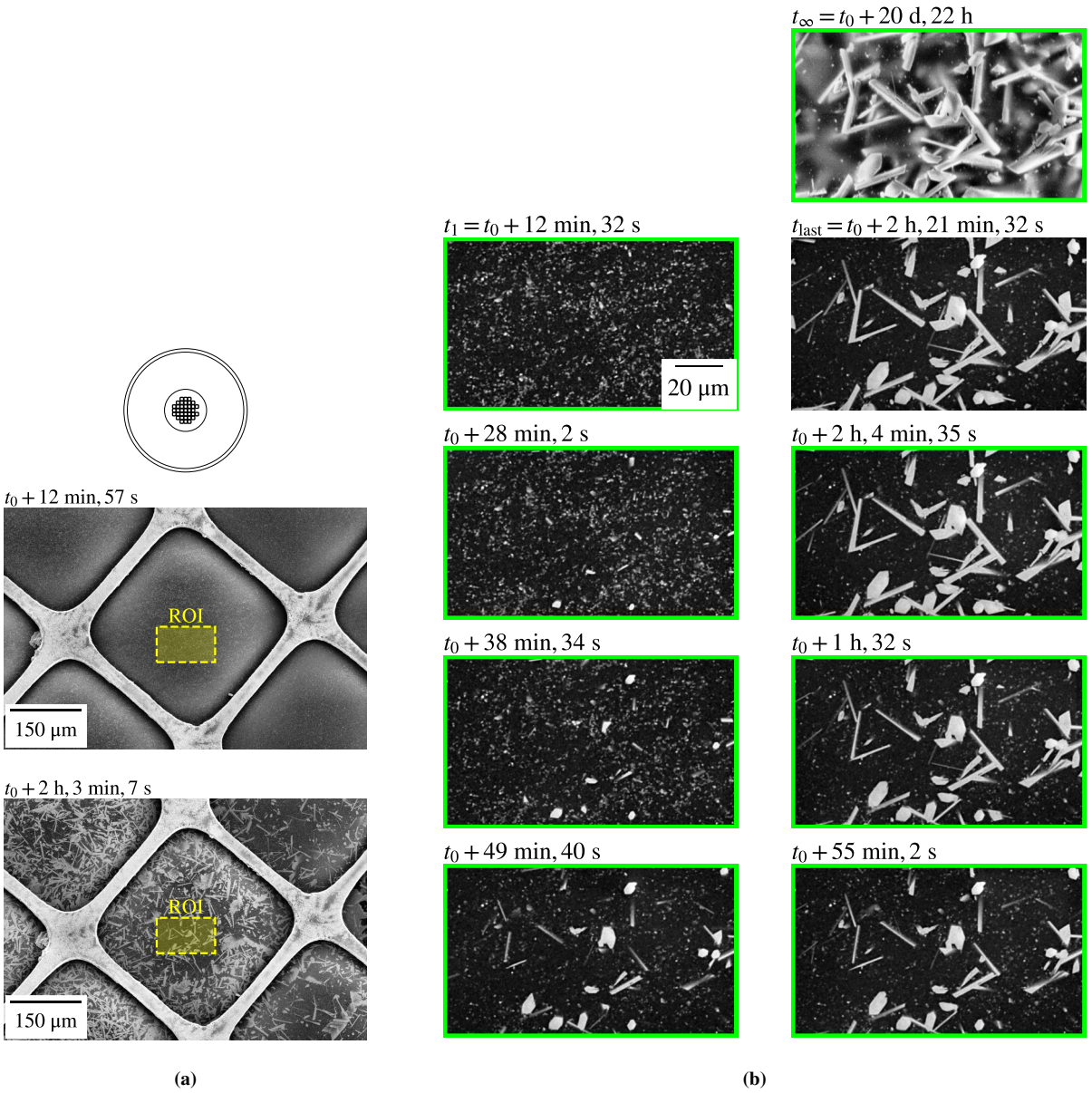

Figure 3: *In situ* micrographies of gypsum plaster crystals growing with citric acid in QX202C cell from experiment 4. For experiment details, refer to table 1. **(a)** Overview of the grid and location of the region of interest (ROI) 13 min (above) and 2h (below) after t_0 and **(b)** Zoom in the ROI monitored at different times (including t_1 and t_{last}, times of first and last images, respectively, and t_∞, collected many days after at the same location). A timelapse obtained from the micrographies of an equivalent experiment (experiment 1) can be found in [20]. Reproduced from doi: 10.6084/m9.figshare.23723673

particles, is described below. Whereas it is easy to distinguish particles from the dark background based on gray levels, HH and DH particles can be segmented neither on the basis of their relatively similar gray levels, nor on the basis of their morphology. Especially in the first images (*i.e.*, for $t <\approx 30$ min), it is likely that both HH and DH particles should be seen at this stage, but that DH is not crystallized enough yet to its well-known shapes (needle, platelet).

To overcome this issue, segmentation of HH particles was performed based on the fact that their surface area should decrease with reaction time as they dissolve during plaster setting (see eq. (1)). HH binary mask was built for each analyzed raw image (named with a R), as illustrated in figs. S4 and S5 and detailed in supplementary information. To obtain DH masks, segmentation of DH crystals was performed by subtracting the HH masks from the corresponding binary images (named with A in figs. S4 and S5). This methodology can be validated by superimposing both HH and DH masks to their corresponding raw images. The fig. 4 shows that the evolution of the HH (with red contours) and the DH (with blue contours) are consistent with micrographies at different stages of the setting reaction. Moreover, few HH particles are identified, and their dissolution process can not be monitored in these experiments. However, the fig. 4 highlights the interest of the method developed in this work to study the growth of DH crystals.

In the following, the extent of the setting reaction will be modelled by the surface fraction occupied by precipitating DH crystals ($\phi_{\mathrm{wp}}(t)$). $\phi_{\mathrm{wp}}(t)$ is computed at any time t from binary DH masks by dividing the number of white pixels ($n_{\mathrm{wp}}(t)$) contained in the DH contours by the total number of pixels in the binary image (n_{p}), see eq. (2).

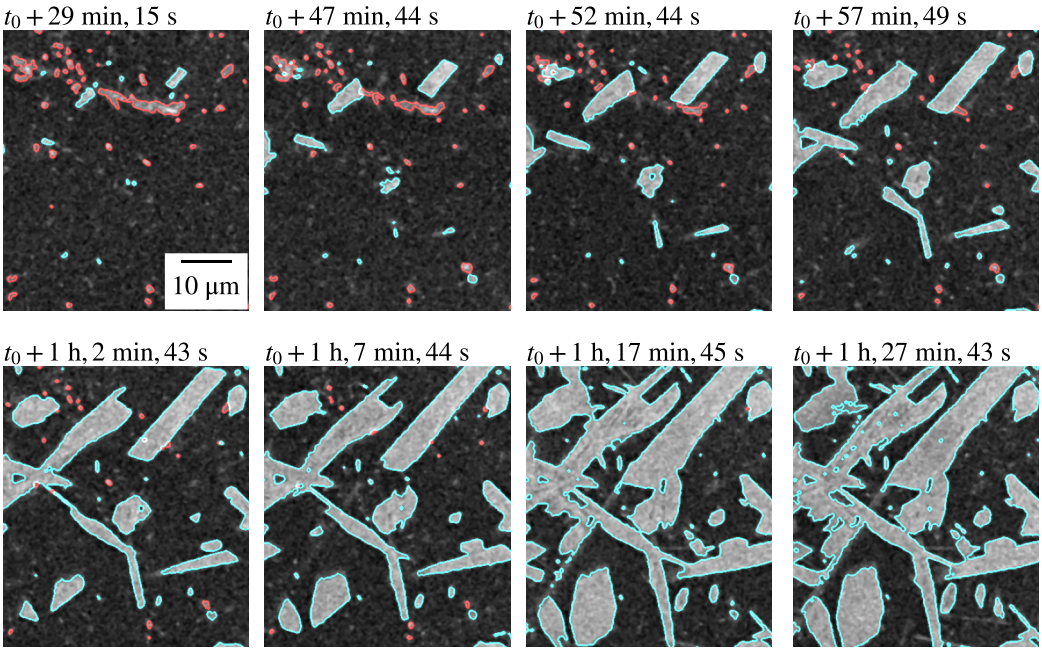

Figure 4: Image sequence of a fraction of the collected area from experiment 1 (5.2 mM citric acid). For experiment details, refer to table 1. After segmentation, HH and DH crystals can be correctly identified, respectively with red and blue outlines. Reproduced from doi: 10.6084/m9.figshare.23723673 © (2023) A. Fantou, CC BY 4.0 license `https://creativecommons.org/licenses/by/4.0/`.

$$\phi_{\mathrm{wp}}(t) = \frac{n_{\mathrm{wp}}(t)}{n_{\mathrm{wp}}(t) + n_{\mathrm{bp}}(t)} = \frac{n_{\mathrm{wp}}(t)}{n_{\mathrm{p}}} \tag{2}$$

with ϕ_{wp} the surface fraction occupied by white pixels, n_{wp}, n_{bp} the number of white and black pixels, respectively, and n_{p} the total number of pixels.

In order to compare different experiments, with different surface crystal fractions in the observation area, a normalized surface density is computed as in eq. (3):

$$\overline{\phi_{\mathrm{wp}}}(t) = \frac{\phi_{\mathrm{wp}}(t)}{\max\left(\phi_{\mathrm{wp}}(t)\right)} \tag{3}$$

with $\overline{\phi_{\mathrm{wp}}}$ the normalized surface fraction occupied by white pixels. The normalization is done respectively to the maximum value of ϕ_{wp} reached at plateau.

Figure 5 shows the evolution with time of the normalized surface fraction of DH crystals $\overline{\phi_{\mathrm{wp}}}(t)$. For a better comparison of the qualitative observations with the quantitative evolution plotted in fig. 5, the magenta and green squares indicate the times at which micrographies displayed in figs. 2 and 3 were collected. As already observed in fig. 2, the DH crystals have already significantly grown at t_1 ($\overline{\phi_{\mathrm{wp}}}(t_1) \approx 0.5$). Thus, it is impossible to monitor the beginning of the setting reaction without the use of any retardant. As expected, the presence of citric acid delays the beginning of the precipitation of DH crystals: red curves all show a time shift compared to the blue ones. The 5 red curves, computed from plaster setting in the presence of citric acid, highlight the reproducibility of the experiments in terms of times. Three regimes are observed and three characteristic times can be defined based on these regimes:

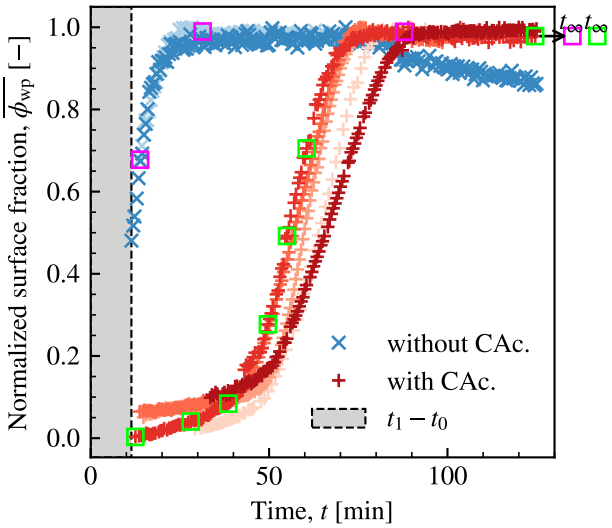

Figure 5: Evolution of the normalized surface fraction of white pixels $\overline{\phi_{\mathrm{wp}}}$, between t_1 and t_{last}. Blue crosses and red plus markers represent experiments conducted without ($N = 2$, pale and dark blue) and with ($N = 5$, different shades of red) citric acid (CAc.), respectively. For experiment details, refer to table 1. $\overline{\phi_{\mathrm{wp}}}(t_\infty)$ was not computed as micrographies at t_∞ were recorded with different conditions, several days after t_{last}. The magenta and green squares highlight times at which were collected the micrographies displayed in figs. 2(b) and 3(b), respectively. The gray area represents the dead-time between the mixing time t_0 and the first acquisition t_1. The evolution of the (non-normalized) surface fraction ϕ_{wp} is displayed in fig. S1. Reproduced from doi: 10.6084/m9.figshare.23723673 © (2023) A. Fantou, CC BY 4.0 license `https://creativecommons.org/licenses/by/4.0/`.

- during the induction period, the solid fraction of DH crystals slowly evolved up to the time t_2 (end of the induction regime, see fig. S2 for the definition of characteristic times), when the increase of $\overline{\phi_{wp}}(t)$ accelerated;
- time t_3 was defined as the inflexion point in the acceleration regime (see fig. S2);
- after time t_4, the termination regime started as $\overline{\phi_{wp}}(t)$ reached a plateau ($\overline{\phi_{wp}}(t) \longrightarrow 1$): the growth of DH crystals slowed down until no more significant change could be detected. Only in the experiment 2' (in dark blue, without citric acid), $\overline{\phi_{wp}}(t)$ decreased ≈ 50 *min* after t_4. This was probably due to an artifact arising from a shift in contrast in the images acquired after more than 80 min.

The non-normalized surface fraction of DH crystals, $\phi_{wp}(t)$, is also plotted in fig. S1. In addition to what was already seen from the evolution of the normalized surface fraction $\overline{\phi_{wp}}(t)$, it also highlights the dispersion of the final surface fraction of DH crystals between the different experiments. Indeed, $\phi_{wp}(t_{last})$ ranged from $\approx 20_{surf}\%$ to $\approx 75_{surf}\%$. This is explained by the relatively small surface areas monitored during the *in operando* acquisitions and by the variation of local densities in terms of crystals from one region to one another (see for example fig. 3(a)).

To provide quantitative data on the kinetics of the setting reaction, the growth rate of DH crystals $\frac{\partial \phi_{wp}}{\partial t}$ was measured at time t_3, *i.e.*, the inflexion point in the acceleration regime (see fig. S2 for the definition of characteristic times). Table 2 summarizes this DH growth rate $\frac{\partial \phi_{wp}}{\partial t}(t_3)$, as well as all other quantitative data obtained from experiments performed with citric acid. Once again, the reproducibility of the experiments in terms of times is highlighted by the relatively small dispersions between the 5 values of t_2, t_3 and t_4, respectively. When the induction regime ends at t_2, DH crystals occupied $\approx \frac{1}{5}$ of their surface area at the end of the setting reaction ($\overline{\phi_{wp}}(t_2) \approx 0.20$). For all of the 5 experiments, the inflexion point of the acceleration regime was reached when DH crystals had grown to $\approx \frac{1}{2}$ of their final surface area ($\overline{\phi_{wp}}(t_3) \approx 0.55$). Regarding the kinetics of the DH growth, $\frac{\partial \phi_{wp}}{\partial t}(t_3)$ ranges from 1.6% min^{-1} to 3.1% min^{-1}.

Furthermore, a quantitative analysis of gypsum crystals growth can be performed. To display the evolution with time of DH crystals, a superimposition of all their successive contours along one experiment is

Table 2: Characteristic times t_2 (end of induction regime (I)), t_3 (inflection point in the acceleration regime (II)) and t_4 (start of termination regime (III)) determined from curves displayed in fig. 5 for all experiments with citric acid. Mean values and standard-deviations (std) were computed for each parameter ($N = 5$). For experiment numbers and details, refer to table 1. These characteristic times were computed using the second derivative of $\overline{\phi_{wp}}$: $\frac{\partial^2(\overline{\phi_{wp}})}{\partial t^2}$, as illustrated in fig. S2. ϕ_{wp} and $\overline{\phi_{wp}}$ are the surface fractions of white pixels at given times, non-normalized and normalized with respect to the maximum value of ϕ_{wp} reached at plateau, respectively.

	(I)			(II)				(III)		
Exp.	t_2 [min]	$\phi_{wp}(t_2)$ [%]	$\overline{\phi_{wp}}(t_2)$ [–]	t_3 [min]	$\phi_{wp}(t_3)$ [%]	$\overline{\phi_{wp}}(t_3)$ [–]	$\frac{\partial(\phi_{wp})}{\partial t}(t_3)$ [% min^{-1}]	t_4 [min]	$\phi_{wp}(t_4)$ [%]	$\overline{\phi_{wp}}(t_4)$ [–]
1	52.59	9.01	0.17	65.47	29.88	0.55	1.77	77.55	50.50	0.93
2	52.42	7.28	0.20	60.44	18.72	0.52	2.01	76.48	35.65	1.00
3	45.98	8.48	0.18	58.70	26.47	0.56	2.88	71.43	44.48	0.95
4	46.15	4.42	0.21	56.23	11.59	0.54	1.63	67.44	19.34	0.90
5	53.66	15.83	0.23	68.28	39.58	0.57	3.09	83.82	64.12	0.92
Mean	50.16	9.00	0.20	61.83	25.25	0.55	2.28	75.34	42.82	0.94
Std	3.37	3.76	0.02	4.43	9.57	0.02	0.59	5.58	14.95	0.03

shown in fig. 6(a) (in black) and in fig. 6(b) (colors changing with time t). These images combine information on crystal shape, growth direction and kinetics. As the time step between two acquired images is constant in a sequence, large distances between successive contours are indicative of fast crystal growth.

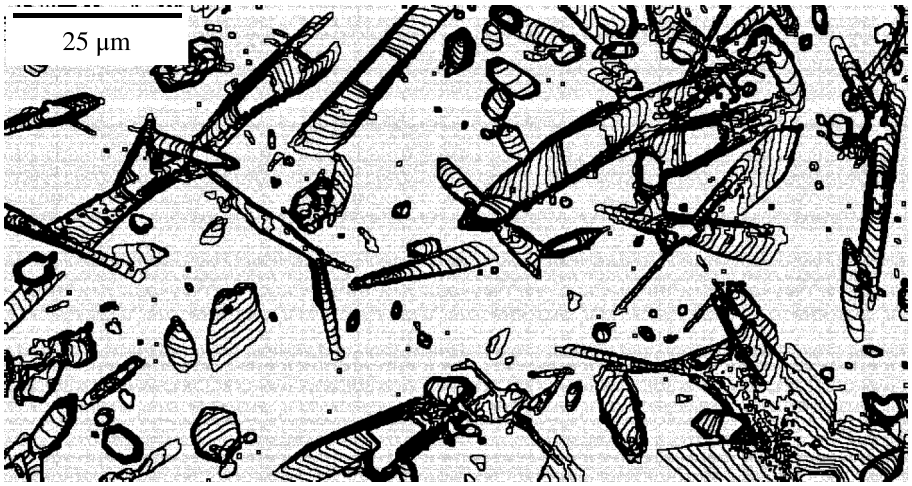

(a)

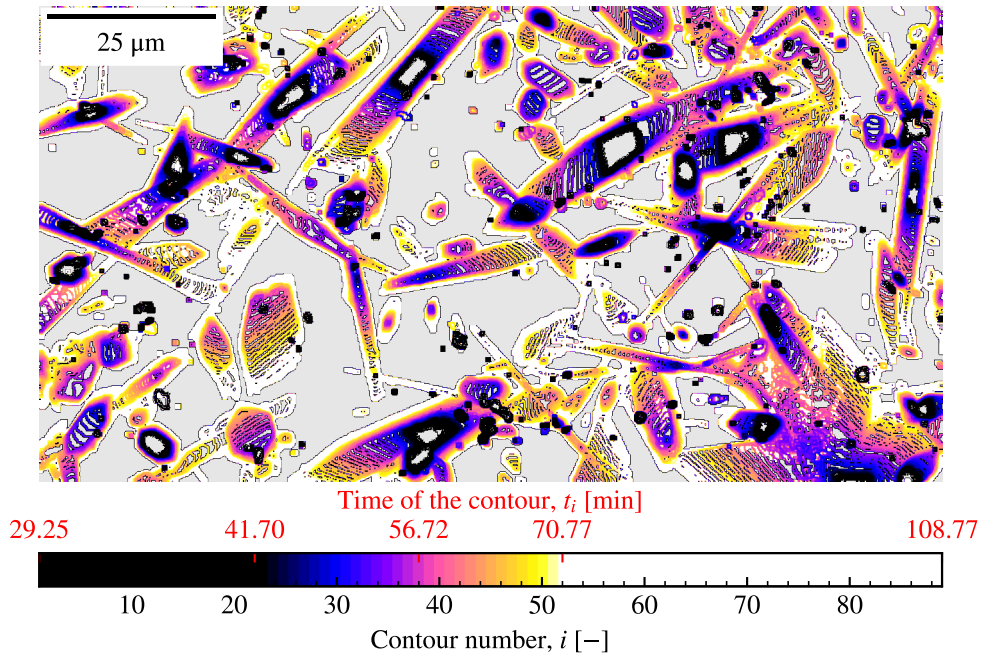

(b)

Figure 6: Evolution of DH crystals contours with time, from experiment 1 with citric acid. For experiment details, refer to table 1. **(a)** focus on the beginning of the crystal growth: superimposition of DH contours from 42 min to 70 min (constant time step between 2 successive contours, t_{step} = 2 min); **(b)** superimposition of all the DH contours up to t_{last}. Time scale is displayed by the colors gradation and by the increase of contour number i (constant time step between 2 successive contours, t_{step} = 1 min). Reproduced from doi: 10.6084/m9.figshare.23723673 © (2023) A. Fantou, CC BY 4.0 license `https://creativecommons.org/licenses/by/4.0/`.

On the contrary, close lines or contours superimposed on each other mean that the growth rate was low or even negligible, as is generally the case below t_2.

From fig. 6(b), DH crystals can be classified into at least four categories according to their growth modes: longitudinal growth or isotropic mode, growth from an apex, or from a side of the crystal. These different growth modes may be explained by different crystal orientations.

To further investigate this issue, six isolated DH crystals with longitudinal growth mode have been chosen from experiments 1 and 2 (refer to table 1 for experiment details). Their length and width have been measured over about 100 images collected during each experiment. The evolution of the crystal dimensions with time is plotted in figs. 7(a) and 7(b). Interestingly, their evolution is similar and three growth regimes can be identified. In regime (I), the length increased slowly when compared to regime (II), during which the longitudinal growth rate reached a typical value of 18 nm/s. On the contrary, the crystal width increased linearly with time, with no change in velocity between regimes (I) and (II) (fig. 7(b)). In regime (III), the growth stopped, most probably due to crystals coming into contact with others, as supported by fig. 6(b). It is also noteworthy that the transitions from regimes (I) to (II), and from regimes (II) to (III), occurred at approximately constant times, respectively $t \approx 50$ min and $t \approx 75$ min to 80 min.

Figure 7(c) displays the shape of one of the six isolated DH crystals, at times $t = 35$ min (regime (I)) and $t = 1$ h, 4 min (regime (II)). The change in the angles measured directly on the DH contours (see fig. 7(c)) was concomitant with the transition from regimes (I) to (II), which appears to be indicative of crystal structure changes. To identify the crystallographic planes in regime (II), data from the literature describing DH crystal facets at equilibrium [22, 23] can be used. We also have to take into account the fact that the DH contours are obtained from top-views of the crystals. Hence, the edges of the contours do not necessarily correspond to real facets but may actually correspond to the projection of facets onto the plane of the QuantomiX cell membrane. With this in mind, DH crystals were modeled with the software Vesta [24] using the $C\,2/c$ monoclinic structure from [25] (see figs. 7(d) and 7(e)).

An excellent agreement is found between the experimental contours (fig. 7(c)) and the crystal top views (fig. 7(d)), with long and short sides defined from the intersection of {120} and {111} facets, respectively. It is noteworthy that the {010} facet was the one in contact with the cell membrane. This is consistent with the fact that the cell membrane is hydrophilic and that water molecules in DH crystals are organized in planes corresponding to {020} facets.

Based on the indexation for the crystal structure in regime (II), an indexation can be proposed for the DH crystal in regime (I), with the same zone axis. Obviously, the longest sides of the crystal already corresponded to the intersection of {120} facets. However, for the shortest sides, no agreement could be found between the planes present in the crystal at equilibrium and the experimental contour (fig. 7(c)). From the value of the angles, we hypothesize that the shortest sides corresponded to the projection of {445} or {455} planes. As these planes are not thermodynamically stable but very similar to {111} obtained at equilibrium, this could explain the transition from regime (I) to regime (II).

Similarly, the indexation of several crystals, growing either longitudinally, or isotropically, or from a side, is summarized in fig. 8. For each crystal, the indexation at the end of the setting reaction contains only the equilibrium facets described in the literature [22, 23]. Misorientations between the models and the experimental angles of the DH contours remained below 14° (mostly below 10°), comforting the hypotheses made for the indexation of the facets.

Finally, growth rates were determined for each specific crystallographic plane identified previously, and for all growth regimes, using the evolution of DH contours with time. To account for the fact that not all growing facets were parallel to the cell membrane, the measured apparent growth rates have been corrected to obtain average growth rates in the perpendicular direction to the considered facets (see fig. 8).

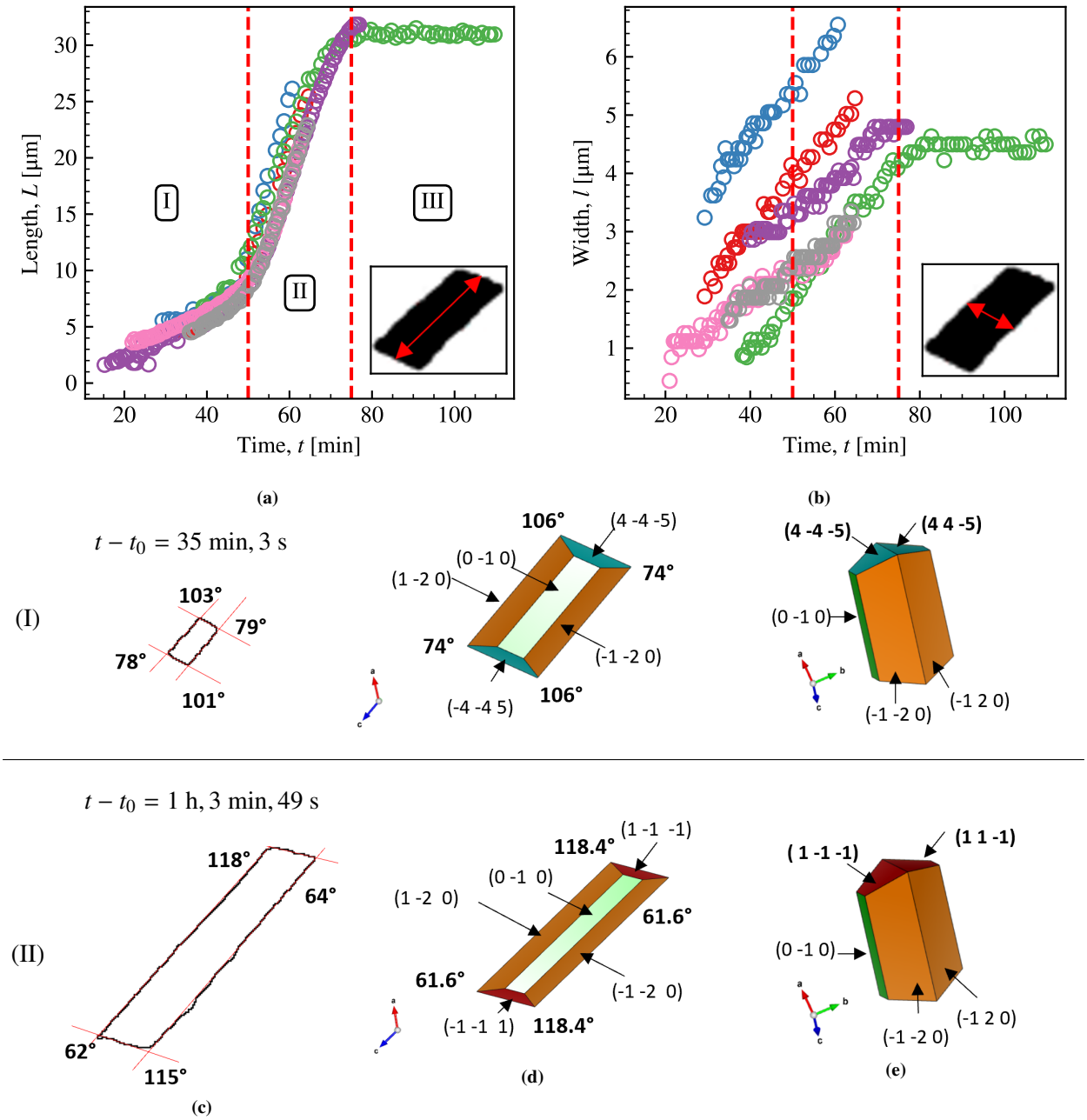

Figure 7: Evolution with time of 6 DH crystals following a longitudinal growth; crystals from experiments 1 to 5, with citric acid. **(a)** Evolution of the length of DH crystal versus time $N = 6$. **(b)** Evolution of the width of DH crystal versus time $N = 6$. **(c)** Experimental measurements of angles of a typical DH crystal. **(d)** 2D and **(e)** 3D views (built with Vesta software [24]) of the crystallography of a typical DH crystal. Crystal modelization was based on the experimental angles and 2D morphology and on the equilibrium facets. Reproduced from doi: 10.6084/m9.figshare.23723673 © (2023) A. Fantou, CC BY 4.0 license https://creativecommons.org/licenses/by/4.0/.

	Longitudinal growth	Isotropic growth	Growth from one side
	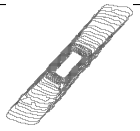		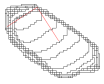
Regime I	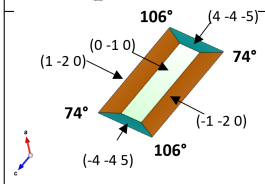	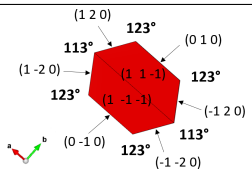	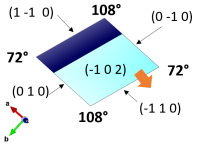
Regime II	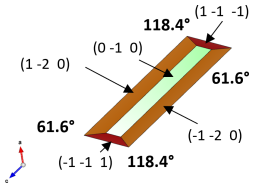		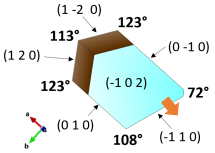
Regime III			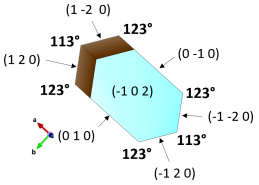
	Average growth rate [nm/s]		
{120}	$0.6^{[I,II]}$	0.6	$0.9^{[II,III]}$
{010}	–	0.5	$0.7^{[I,II,III]}$
{110}	–	–	$13^{[I,II]}$
{111}	$7.6^{[II]}$	–	–
{4 – 45} or {4 – 5 – 5}	$1.9^{[I]}$	–	–

Figure 8: Typical DH crystal indexation for 3 different types of crystal growth (longitudinal, isotropic or growth from one side) and measured average growth rates of crystal planes. In this work, DH crystals were studied from experiments 1 to 5, with citric acid. Reproduced from doi: 10.6084/m9.figshare.23723673 © (2023) A. Fantou, CC BY 4.0 license `https://creativecommons.org/licenses/by/4.0/`.

4. Discussion

The aims of this study were:

- to implement a robust methodology for the *in operando* monitoring at micro-scale of the evolution of the microstructure of hydraulic binders during their setting process and with a L/S used in application;
- to characterize the setting of gypsum plaster through the observations of the dissolution of HH particles and the precipitation of DH crystals;
- to quantify the kinetics of the dissolution and precipitation reactions from image analysis, with sufficient temporal and spatial resolutions;
- to better understand the mechanisms of nucleation and growth of individual DH crystals in relation to their crystallography.

The use of encapsulating cells enabled to investigate the evolution of setting pastes in conditions close to the ones in application (*e.g*, pressure, temperature, liquid to solid mass ratio) and with a very good spatial resolution (pixel size of $\approx$ 100 nm). The protocol used in this work enabled a precise control of the L/S ratio and thus of the supersaturation reached in the paste when HH particles dissolve. Both these parameters have a strong influence on the kinetics of the reactions and on the development of the microstructure one aims to follow. Indeed, in such concentrated pastes, growing DH crystals eventually contact or/and entangle with each others (see fig. 6), which may influence their later growing mechanism.

To observe setting processes in SEM without the use of such sealed cells, it would have been necessary to stop the setting process, for instance by immersion of the setting paste in a solvent such as ethanol [3, 26, 27]. This would enable SEM observation with a good resolution but without the possibility to follow the evolution of the microstructure of a same sample, and with a risk of affecting it due to the quenching protocol. The monitoring of dissolution and precipitation in liquid-phase STEM-in-SEM (Scanning Transmission Electron Microscopy) is also possible, but it requires very dilute conditions and is thus more distant from the real conditions of application of hydraulic binders [28]. Finally, the method developed in this work appears to be complementary to other techniques:

- X-ray tomography with concentrated pastes representative of the application and enabling a characterization of the bulk of the setting paste with 3D measurements [16, 17], but with a degraded spatial resolution;
- AFM to follow the dissolution/precipitation in very diluted suspensions, with a very good resolution at the scale of single crystals, not entangled and without control of the amount of liquid [11–15].

Because of the dead-time needed for the sample preparation, and probably also due to the design of the environmental cell , few HH particles were identified (represented with red outlines in fig. 4). Thus, it was not possible to quantify the kinetics of their dissolution. On the bright side, the method developed in this work proved to be very efficient and with sufficient time and spatial resolutions to study in detail the growth of relatively small DH crystals evolving quickly. This dynamic process was quantified by image analysis both at a microscale (ROI containing more than a hundred DH crystals, fig. 5) and at the scale of individual DH crystals (fig. 7). Kinetics measured at the microscale provided mean values, less sensitive to heterogeneities in particles, while follow-up of individual crystals permitted to relate their growth regimes to changes in crystallography . This is especially interesting as data is lacking on precipitation mechanisms and discrepancies still exist in the literature. For instance, while in some studies DH crystals are thought to nucleate on dissolving HH particles [8], others advocate for a nucleation of DH crystals nearby HH particles, in confined supersaturation regions [16–18].

4.1. Representativeness of the in operando observations

Even if the methodology was carefully designed in order to minimize any effect on the observed transformation and kinetics, the representativeness of results obtained from these *in operando* setting experiments should be addressed before extrapolating these results to gypsum plasters used in applications. First, due to the protocol, t_1 could not be smaller than 10 to 15 min. Hence, it was necessary to use citric acid as a setting retardant to be able to monitor the reaction since its beginning. Indeed, the fig. 5 shows that, without any retardant, the reaction was already too advanced at $t = t_1$. However, it should be taken into account that the addition of citric acid may influence the growth regimes and rates of DH crystals [29–31].

Second, the experiments were carried on a small volume of paste (7 µL in the Quantomix QX202C). Due to the exothermic character of the setting reaction, its kinetics could be slowed down compared to bigger volumes of setting plaster [8].

With the methodology developed here, the reaction kinetics was repeatable (see fig. 5). However, from one experiment to another one, the surface fraction reached at t_{last} varied from 20 $_{\text{surf}}$% to 75 $_{\text{surf}}$% (see fig. S1). Indeed, the local crystal density was observed to be heterogeneous depending on the chosen region of interest (ROI) on a same cell (see fig. 3(a)). We believe that it may be due to variations in the sample preparation: the concentration of the two drops successively pipetted within a larger volume of setting paste and their deposit on the membrane without the possibility to further homogenize it.

In the following, to better discuss its representativeness, the experimental surface fraction reached at t_{last} within the setup was compared to the expected surface fraction of solid, computed from the setting reaction (see eq. (1)), and to an experimental surface fraction of solid measured from X-ray tomography acquisitions on *ex situ* set samples. From eq. (1), if one considers the volume fraction of void (*i.e.*, pores) to arise from the excess water and the volume shrinkage (due to the mass density difference between HH and DH), it comes that the volume fraction of solid (*i.e.*, crystals) once the reaction is completed can be expressed as in eq. (4).

$$\Phi_{\text{solid}}\left(\frac{L}{S}\right) = \frac{\frac{M_{\text{DH}}}{M_{\text{HH}}} \times \frac{\rho_{\text{H}_2\text{O}}}{\rho_{\text{DH}}}}{\left[\frac{L}{S}\right] + \frac{\rho_{\text{H2O}}}{\rho_{\text{HH}}}} = \frac{0.51}{0.60 + 0.38} = 0.52 \tag{4}$$

with Φ_{solid} the volume fraction of solid (*i.e.*, crystals), M_{DH}, M_{HH} the molar masses of calcium sulfate dihydrate and hemihydrate, repectively (*i.e.*, bassanite and gypsum) and $\rho_{\text{H}_2\text{O}}$, ρ_{DH} the mass densities of water and calcium sulfate dihydrate, respectively. With the used L/S ratio, it comes that the expected final volume fraction of solid is $\Phi_{\text{solid}} = 52$ $_{\text{vol}}$%. If the density of the material is homogeneous and isotropic, then the surface fraction of solid should be strictly equal to the volume fraction of solid. Thus, $\phi_{\text{sol}} = \Phi_{\text{sol}} = 52$ $_{\text{surf}}$%.

Complementary, X-ray tomography acquisitions were performed, focusing on the core of samples of gypsum plaster set *ex situ* (*i.e.*, out of any cell) with citric acid. From a same 3D reconstruction, eleven 2D cross sections of surface areas equivalent to the ones analyzed in SEM experiments, *i.e.*, (130×70) µm^2 were selected randomly. The fig. S3 exhibits the results of the analysis of the surface fraction of solid of these cross sections. It is shown that on 11 cross sections, the surface fraction of solid varied from $\phi_{\text{sol}} = 51$ $_{\text{surf}}$% to $\phi_{\text{sol}} = 73$ $_{\text{surf}}$%, with a mean value of $\phi_{\text{sol}} = (60.6 \pm 8.2)$ $_{\text{surf}}$%. It is worth noting that the total volume fraction of solid in the whole sample was determined to be 59 $_{\text{vol}}$%. With these results, we can reasonably consider that experiments in which the final surface fraction of solid was within 50 $_{\text{surf}}$% and 60 $_{\text{surf}}$% (fig. S1) were representative of real conditions. Moreover, this does not seem to be critical since the aim of this study was not to quantitatively measure the volume fraction of gypsum plaster, which is more conventionally characterized by X-ray tomography or mercury intrusion porosimetry.

4.2. Potential artifacts induced by the developed methodology

Due to the presence of the electron beam, irradiation damage in the setting paste may be expected and cause artifacts as it is known to induce water radiolysis [32, 33]. Irradiation damage may generate reactive species, such as aqueous electrons e^-_{aq}, or protons and other species as H^+, OH^-, $H^\cdot$, $OH^\cdot$. These species can change the solution pH , and thus influence the reaction mechanisms characterized in this paper [8]. In order to limit its influence, the electron beam was blanked between each acquisitions (taken every 30 s then every 1 min). In these conditions, no obvious signs of irradiation damage were visible in the monitored region. Moreover, the comparison with non-irradiated regions of the encapsulating cell , observed either during or after the setting reaction, has shown no significant difference, which could be allocated to the electron beam (*e.g.*, similar crystals morphologyand density).

Even with a quite large depth of field, the crystals that were imaged were the ones located at the surface of the cell, close to the membrane. Monte Carlo simulations (*cf.* table S1) suggested that the probed depth was about 200 nm below the membrane. Therefore, DH crystals nucleating below the probed depth would not be detected from the beginning and may become visible only when they grow up sufficiently for their extremity to become close enough to the membrane, being then counted as new nuclei. However, it did not seem to be the case for many DH crystals (fig. 4).

This is consistent with the expected preferential orientation of DH crystals nucleating and growing close to the surface, owing to the presence of the cell membrane and to its hydrophilic nature. Even though the cell membrane was not rigid (see its curvature in fig. 1), its presence may have affected the orientation of the DH crystals, with an expected preferential orientation of {010} facets parallel to the membrane.

All this highlights the importance of combining characterization techniques, at different scales, to draw the whole picture and provide explanations on the setting mechanisms.

4.3. Crystal indexation and atomic plane growth rates

These *in operando* SEM experiments provided information on the crystallization stages of gypsum and their kinetics. Indeed, in the case of retarded samples, for which the induction period could be observed, the normalized surface fraction of gypsum exhibited a three-stage evolution with time, describing a sigmoid curve (see fig. 5). The first regime corresponded to slow germination of the crystals and lasted until $t \approx 50$ min. Then, in a second regime, these crystals were observed to grow more rapidly. The rate of the solid fraction in the different ROI, given by the slopes of the non-normalized curves (table 2) ranged from 1.6 $_{\text{surf}}$%/min to 3.1 $_{\text{surf}}$%/min. At a certain point, the crystal growth slowed down and the surface fraction of gypsum reached a plateau at $t \approx 75$ min to 80 min corresponding to the third regime.

These variations in growth rates at the microscopic level are also evidenced by electron microscopy images (fig. 6(b)). Regime (I) corresponds to crystals with black outlines: contours are close to each others, indicating that the crystals evolved slowly. Then, during the regime (II), the crystals grew rapidly (blue, pink then yellow contours), before reaching a stable size, corresponding in most cases to contacts between each crystal. Interestingly, the regimes corresponded exactly to the ones defined at the macroscopic level. In fig. 6, we can see that the majority of the crystals visualised in 2D are longitudinally growing needles. Other crystals, a minority in number and surface area, have an isotropic growth, or grew from an edge or an apex. It can therefore be assumed that the rate of surface densification was directly related to the rate of growth of longitudinal crystals. It can also be considered that most of the crystals visible on the images correspond to needles seen under different orientations.

The changes in crystal growth rates from regime (I) to regime (II) was associated to crystalline modifications (fig. 7). Indexations of the crystal facets have been suggested, considering that the shape of the crystals after long reaction times (hence in regime (II)) corresponded to their shape at equilibrium [22, 23]. The indexation of {120} and {010} facets was straightforward as they are well known in the literature. In regime

(I), more exotic {445} or {455} planes have been evidenced. The presence of unstable planes in regime (I) could be evidenced here thanks to the developed methodology combining *in operando* and nanometer-scale spatial resolution. The transformation from {445} or {455} planes to {111} planes, with almost similar Miller indices, supports the proposed indexation.

As far as the growth rates of crystallographic planes are concerned (fig. 8), it is difficult to draw a comparison with values given in the literature, in which growth rates were usually measured using AFM on diluted solutions. It is indeed known that the growth rates depend on solution supersaturation [9], and, to our knowledge, this is the first *in operando* study, in which growth rates of DH crystalline planes was measured in concentrated plaster pastes (L/S representative of industrial applications). For instance, {010} facets were sometimes qualified as stable, with a slow growth [10] and as very reactive in other studies [11]. Such discrepancies may arise from different experimental conditions (especially L/S ratios). However, it is generally accepted that the {120} facets of DH crystals are stable, whereas the {111} are less stable and grow fast [10, 11]. Also, the growth rate of {010} facets is known to be reduced in the presence of Na-citrate retardant [9]. The main advantages of our experiment lies in the fact that this non-destructive method enables the *in operando* follow-up of a same sample throughout the whole setting process with a liquid phase representative from the real plaster setting (L/S, excepted for the presence of retardant). Being able to quantify the DH growth rates in conditions representative of application is particularly important as it is known to govern the development of the microstructure during setting, the entanglement of DH crystals and of intercrystalline bonds, which in turn play a critical role in the mechanical properties of the final material.

5. Conclusions

The *in operando* SEM study of the precipitation of gypsum crystals from the dissolution of calcium sulfate hemihydrate particles was made possible in standard conditions by the use of a specific encapsulating cell without and with citric acid (5.2 mM). The size of the observed region was typically (130×70) μm^2 with a resolution of 139.6 nm, which enabled to monitor the evolution of dozens of crystals. Image analysis based on segmentation provided quantitative results on the growth of crystals at global (*i.e.*, region of observation) and local (*i.e.*, single crystal) scales. Different crystal growth regimes were observed (*e.g.*, longitudinal, isotropic, from a side) due to different crystal orientations. An indexation of single crystal facets based on crystallography and litterature results was proposed and the crystal growth rates were measured for 5 crystallographic planes. It was found that:

- the {111} and {110} planes were the fastest growing planes, with growth rates of $\approx$ 8 nm/s and $\approx$ 13 nm/s, respectively;
- the {120} and {010} planes were the most stable and grew slowly at similar rates of $\approx$ 0.7 nm/s;
- the {4 − 45} or {4 − 5 − 5} were identified as unstable planes, growing at $\approx$ 2 nm/s. Such unstable planes transformed into {111} during the setting, causing a change in the growth regime and kinetics.

Kinetics variations, observed locally at the scale of individual DH crystals, were totally consistent with mean variations measured at the microscopic scale, displaying a sigmoid evolution in three stages (induction, acceleration and termination regimes).

Competing interests

The authors declare none.

Acknowledgements

This work was supported as part of SUN7 project (**S**trUcturi**N**g and **SET**ting processes of mineral cements for bone repair) funded by the French ANR [ANR-19-CE08-0008]. The authors would like to thank Thierry Douillard for his support on SEM techniques, Jérôme Adrien for his support on the X-ray tomography acquisition and the mechanical workshop of Mateis Laboratory for the manufacturing of the QuantomiX cell holders.

Data availability statement

Timelapses gathering raw images (before image analysis) of representative experiments are available from https://hal.science/hal-04168810 and https://hal.science/hal-04168814. Other raw and processed data required to reproduce these findings cannot be shared at this time as the data also forms part of an ongoing study.

References

[1] A. Packter, The precipitation of calcium sulphate dihydrate from aqueous solution, Journal of Crystal Growth 21 (1974) 004–009. doi:10.1016/0022-0248(74)90004-9.

[2] M. E. Tadros, I. Mayes, Linear growth rates of calcium sulfate dihydrate crystals in the presence of additives, Journal of Colloid and Interface Science 72 (1979) 245–254. doi:10.1016/0021-9797(79)90106-1.

[3] A. J. Lewry, J. Williamson, The setting of gypsum plaster – Part II The development of microstructure and strength, Journal of Materials Science 29 (1994) 5524–5528. doi:10.1007/BF00349943.

[4] U. Tritschler, M. Kellermeier, C. Debus, A. Kempter, H. Cölfen, A simple strategy for the synthesis of well-defined bassanite nanorods, CrystEngComm 17 (2015) 3772–3776. doi:10.1039/c5ce00519a.

[5] A. E. S. Van Driessche, T. M. Stawski, L. G. Benning, M. Kellermeier, Calcium Sulfate Precipitation Throughout Its Phase Diagram, Springer International Publishing, Cham, 2017, pp. 227–256. doi:10.1007/978-3-319-45669-0_12.

[6] A. Katz, A. Bentur, K. Kovler, A novel system for in-situ observations of early hydration reactions in wet conditions in conventional SEM, Cement and Concrete Research 37 (2007) 32–37. doi:10.1016/j.cemconres.2006.09.014.

[7] A. E. S. Van Driessche, L. G. Benning, J. D. Rodriguez-Blanco, M. Ossorio, P. Bots, J. M. García-Ruiz, The role and implications of bassanite as a stable precursor phase to gypsum precipitation, Science 336 (2012) 69–72. URL: https://science.sciencemag.org/content/336/6077/69. doi:10.1126/science.1215648.

[8] M. Ilett, H. M. Freeman, Z. Aslam, J. M. Galloway, D. P. Klebl, S. P. Muench, I. J. McPherson, O. Cespedes, Y. Y. Kim, F. C. Meldrum, S. R. Yeandel, C. L. Freeman, J. H. Harding, R. M. D. Brydson, Evaluation of correlated studies using liquid cell and cryo-transmission electron microscopy: Hydration of calcium sulphate and the phase transformation pathways of bassanite to gypsum, Journal of Microscopy n/a (2022). doi:10.1111/jmi.13102.

[9] D. Bosbach, M. F. Hochella, Gypsum growth in the presence of growth inhibitors: a scanning force microscopy study, Chemical Geology 132 (1996) 227–236. URL: https://www.sciencedirect.com/science/article/pii/S0009254196000599. doi:10.1016/S0009-2541(96)00059-9.

[10] C. Hall, D. C. Cullen, Scanning force microscopy of gypsum dissolution and crystal growth, AIChE Journal 42 (1996) 232–238. doi:10.1002/aic.690420119.

[11] E. Finot, E. Lesniewska, J.-C. Mutin, J.-P. Goudonnet, Reactivity of gypsum faces according to the relative humidity by scanning force microscopy, Surface Science 384 (1997) 201–217. URL: http://www.sciencedirect.com/science/article/pii/S0039602897002203. doi:10.1016/S0039-6028(97)00220-3.

[12] E. Finot, E. Lesniewska, J.-C. Mutin, J.-P. Goudonnet, Investigations of surface forces between gypsum crystals in electrolytic solutions using microcantilevers, The Journal of Chemical Physics 111 (1999) 6590–6598. doi:10.1063/1.479950.

[13] E. Finot, E. Lesniewska, J.-P. Goudonnet, J. C. Mutin, Correlation between surface forces and surface reactivity in the setting of plaster by atomic force microscopy, Applied Surface Science 161 (2000) 316–322. URL: http://www.sciencedirect.com/science/article/pii/S0169433200000301. doi:10.1016/S0169-4332(00)00030-1.

[14] E. Finot, E. Lesniewska, J.-C. Mutin, J.-P. Goudonnet, Investigations of surface forces between gypsum microcrystals in air using atomic force microscopy, Langmuir 16 (2000) 4237–4244. doi:10.1021/la9902439.

[15] E. A. Pachon-Rodriguez, A. Piednoir, J. Colombani, Pressure solution at the molecular scale, Phys. Rev. Lett. 107 (2011) 146102. doi:10.1103/PhysRevLett.107.146102.

[16] J. Adrien, S. Meille, S. Tadier, E. Maire, L. Sasaki, In-situ X-ray tomographic monitoring of gypsum plaster setting, Cement and Concrete Research 82 (2016) 107–116. URL: http://www.sciencedirect.com/science/article/pii/S0008884615003051. doi:10.1016/j.cemconres.2015.12.011.

[17] J. Seiller, T. Bonnal, J. Adrien, S. Meille, S. Tadier, E. Maire, A. Bonnin, 4D in situ monitoring of the setting of α plaster using synchrotron X-ray tomography with high spatial and temporal resolution, Construction and Building Materials 304 (2021) 124632. URL: https://www.sciencedirect.com/science/article/pii/S0950061821023874. doi:10.1016/j.conbuildmat.2021.124632.

[18] M. La Bella, R. Besselink, J. P. Wright, A. E. S. Van Driessche, A. Fernandez-Martinez, C. Giacobbe, Hierarchical synchrotron diffraction and imaging study of the calcium sulfate hemihydrate – gypsum transformation, Journal of Applied Crystallography 56 (2023). doi:10.1107/S1600576723002881.

[19] J. Schindelin, I. Arganda-Carreras, E. Frise, V. Kaynig, M. Longair, T. Pietzsch, S. Preibisch, C. Rueden, S. Saalfeld, B. Schmid, J.-Y. Tinevez, D. J. White, V. Hartenstein, K. Eliceiri, P. Tomancak, A. Cardona, Fiji: an open-source platform for biological-image analysis, Nature Methods 9 (2012) 676–682. doi:10.1038/nmeth.2019.

[20] A. Fantou, A. Wozniak, A. Malchère, L. Roiban, S. Meille, K. Masenelli-Varlot, S. Tadier, Timelapse: Crystal growth during setting of gypsum plaster, observed through in-cell environmental SEM (with setting retardant), 2021. URL: https://hal.science/hal-04168810.

[21] A. Fantou, A. Wozniak, A. Malchère, L. Roiban, S. Meille, K. Masenelli-Varlot, S. Tadier, Crystal growth during setting of gypsum plaster, observed through in-cell environmental sem (without any setting retardant), 2021. URL: https://hal.science/hal-04168814.

[22] F. Otálora, J. García-Ruiz, Nucleation and growth of the Naica giant gypsum crystals, Chem. Soc. Rev. 43 (2014) 2013–2026. doi:10.1039/C3CS60320B.

[23] B. Madeja, J. Avaro, A. E. S. Van Driessche, M. Rückel, E. Wagner, H. Cölfen, M. Kellermeier, Tuning the growth morphology of gypsum crystals by polymers, Cement and Concrete Research 164 (2023) 107049. URL: https://www.sciencedirect.com/science/article/pii/S0008884622003416. doi:10.1016/j.cemconres.2022.107049.

[24] K. Momma, F. Izumi, *VESTA 3* for three-dimensional visualization of crystal, volumetric and morphology data, Journal of Applied Crystallography 44 (2011) 1272–1276. doi:10.1107/S0021889811038970.

[25] P. F. Henry, M. T. Weller, C. C. Wilson, Neutron powder diffraction in materials with incoherent scattering: an illustration of Rietveld refinement quality from nondeuterated gypsum, Journal of Applied Crystallography 42 (2009) 1176–1188. doi:10.1107/S0021889809043210.

[26] X. Chen, J. Gao, Y. Zhao, Investigation on the hydration of hemihydrate phosphogypsum after post treatment, Construction and Building Materials 229 (2019) 116864. URL: http://www.sciencedirect.com/science/article/pii/S0950061819323001. doi:10.1016/j.conbuildmat.2019.116864.

[27] C. Liu, J. Gao, X. Chen, Y. Zhao, Effect of polysaccharides on setting and rheological behavior of gypsum-based materials, Construction and Building Materials 267 (2021) 120922. URL: http://www.sciencedirect.com/science/article/pii/S0950061820329275. doi:10.1016/j.conbuildmat.2020.120922.

[28] D. Alloyeau, W. Dachraoui, Y. Javed, H. Belkahla, G. Wang, H. Lecoq, S. Ammar, O. Ersen, A. Wisnet, F. Gazeau, C. Ricolleau, Unravelling kinetic and thermodynamic effects on the growth of gold nanoplates by liquid transmission electron microscopy, Nano Letters 15 (2015) 2574–2581. doi:10.1021/acs.nanolett.5b00140.

[29] C. Vellmer, B. Middendorf, N. Singh, Hydration of α–hemihydrate in the presence of carboxylic acids, Journal of Thermal Analysis and Calorimetry 86 (2006) 721–726. doi:10.1007/s10973-005-7224-4.

[30] K. M. Song, J. Mitchell, H. Jaffel, L. F. Gladden, Simultaneous monitoring of hydration kinetics, microstructural evolution, and surface interactions in hydrating gypsum plaster in the presence of additives, Journal of Materials Science 45 (2010) 5282–5290. doi:10.1007/s10853-010-4572-7.

[31] M. Lanzón, P. A. García-Ruiz, Effect of citric acid on setting inhibition and mechanical properties of gypsum building plasters, Construction and Building Materials 28 (2012) 506–511. URL: http://www.sciencedirect.com/science/article/pii/S0950061811003357. doi:10.1016/j.conbuildmat.2011.06.072.

[32] P. Abellan, T. J. Woehl, L. R. Parent, N. D. Browning, J. E. Evans, I. Arslan, Factors influencing quantitative liquid (scanning) transmission electron microscopy, Chem. Commun. 50 (2014) 4873–4880. doi:10.1039/C3CC48479C.

[33] T. J. Woehl, T. Moser, J. E. Evans, F. M. Ross, Electron-beam-driven chemical processes during liquid phase transmission electron microscopy, MRS Bulletin 45 (2020) 746–753. doi:10.1557/mrs.2020.227.

6. Supplementary information

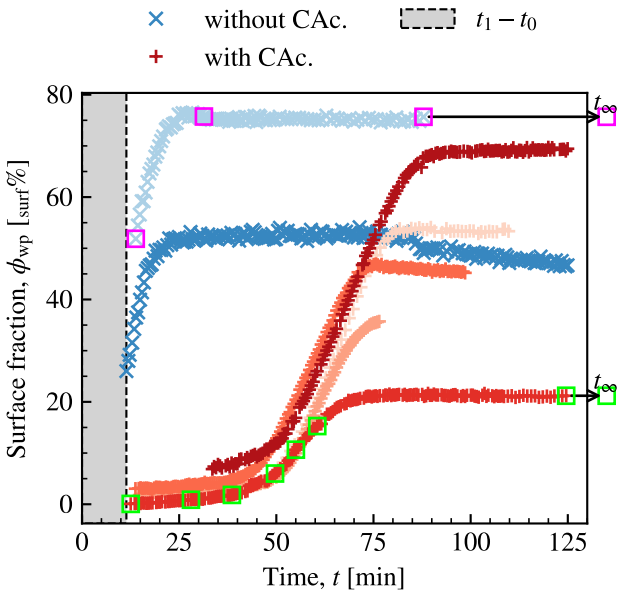

Figure S1: Evolution of ϕ_{wp}, (non-normalized) surface fraction of white pixels for the different experiments, between t_1 and t_{last}. Blue crosses and red plus markers represent experiments conducted without ($N = 2$, pale and dark blue) and with ($N = 5$, different shades of red) citric acid (CAc.), respectively. $\phi_{wp}(t_\infty)$ was not computed as micrographies at t_∞ were recorded with different conditions, several days after t_{last}. For experiment details, refer to table 1. The magenta and green squares highlight times at which were collected the micrographies displayed in figs. 2(b) and 3(b), respectively. The gray area represents the dead-time between the mixing time t_0 and the first acquisition t_1. Reproduced from doi: 10.6084/m9.figshare.23723673

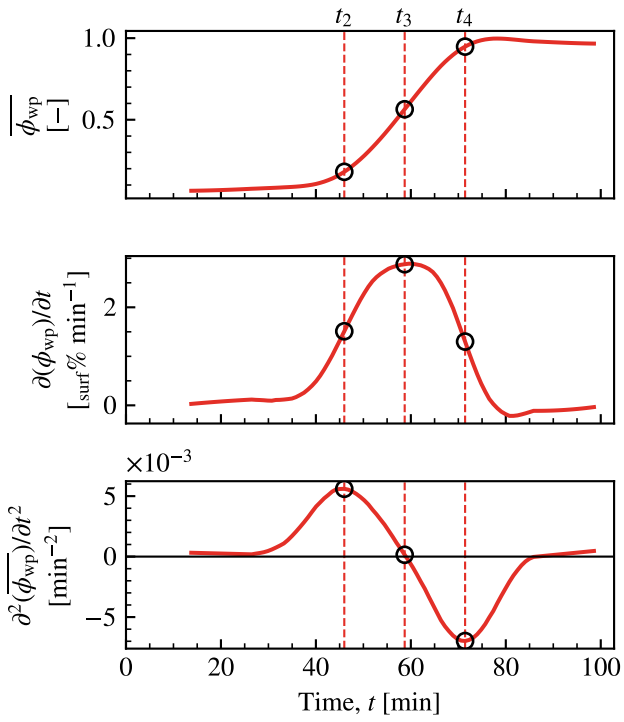

Figure S2: Illustration of the determination of the three characteristic times: t_2 (end of induction regime), t_3 (inflection point in the acceleration regime) and t_4 (start of termination regime: ϕ_{wp} reaches a plateau). These times are chronologically identified when the second derivative of $\overline{\phi_{wp}}$ (surface fraction of white pixels normalized with respect to the maximum value of ϕ_{wp}), $\frac{\partial^2(\overline{\phi_{wp}})}{\partial t^2}$ is maximum, null and minimum, respectively. Computed values of t_2, t_3 and t_4 are provided in table 2. Reproduced from doi: 10.6084/m9.figshare.23723673

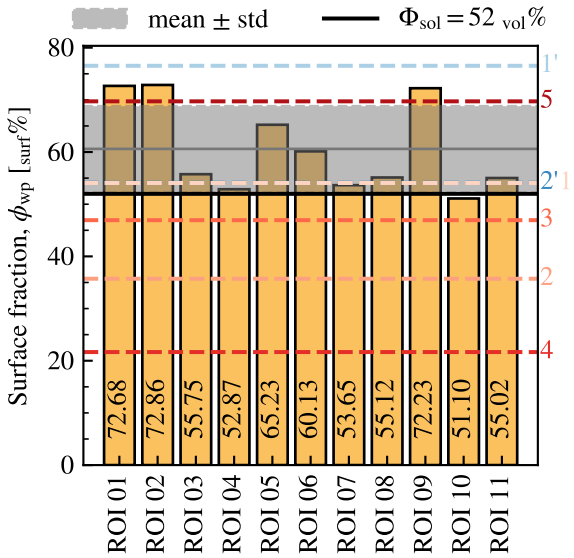

Figure S3: Surface fraction of solid (*i.e.*, crystals) of different ROI arising from 2D slices of a 3D volume obtained from µ-CT. Each ROI has the same dimension (130×70) µm^2, which is equivalent to (433 pix $\times$ 233 pix) for a voxel size of 0.3 µm. The gray range highlights the mean value ± the standard deviation of the surface fractions ($N = 11$). The dashed lines corresponds to the maximum surface fraction reached in the different experiments, which numbers are given on the right (see table 1). The black solid line indicates the theoretical volume fraction of solid Φ_{sol} computed from eq. (4). Reproduced from doi: 10.6084/m9.figshare.23723673

6.1. Details on image processing

Several steps were needed to obtain hemihydrate binary masks. They are described hereafter.

6.1.1. First step: build a binary image for hemihydrate particles from the image acquired at time t_1

A simple threshold was applied on the image stack to separate crystals from the solution (see fig. S4 - R01, R41, A01, A41). At this step, the hemihydrate (HH) particles could not be distinguished from dihydrate (DH) crystals. Indeed, their compositions are quite similar (they differ only by the amount of water molecules), giving the crystals very similar gray levels. To segment the HH particles and not the DH crystals, we considered the fact that HH dissolves during the reaction, whereas the DH germinates and grows in size (see eq. (1)). Hence, by subtracting the binary image corresponding to time t_{41} = 1 h, 3 min, 6 s (A41) to the first binary image (time t_1 = 29 min, 15 s) (A01), pixels corresponding to HH, which disappear during this period of time (t_1 to t_{41}), became black, see A01. The whole HH crystals at time t_1 could then be identified, as they were bound by the contours of image A01 (contours shown in image B01) and contain non-white pixels. Image E was created as the average from images B01 and C. A quick manual filling in black of these HH regions was then carried out. A separation between HH particles and DH crystals (white pixels zones with gray contours in E) was then made by thresholding. The binary image showing HH particles at time t_1 is shown in M. Image F01 shows the overlay of the HH mask with red contours on the SEM image R01.

6.1.2. Second step: build binary masks for hemihydrate particles for each image

This step had to be applied to follow the evolution of HH particles and Dh crystals in function of the reaction time, see fig. S5.

The logical `AND` operation was applied to the binary mask of HH obtained from the image at time t_1 (image M) and each binary image of the first stack (segmented stack, containing all crystals in black on a white background representing the solution) (see fig. S5, images A05 - A20 - A33). The result of this operation correctly matches the evolution of HH particles over time in different images (see F05 and F20), until DH crystals grow and cover the HH areas (see yellow arrows in image F33). In order to fix this issue, we thresholded big needles of gypsum at large times (*e.g.*, $t > t_{30}$). These binary images of DH at times could then be subtracted to the binary images of non-perfect HH. At the end, a binary stack of good quality could be obtained to monitor the evolution of HH particles on the one side (see F′33), and DH crystals on the other side.

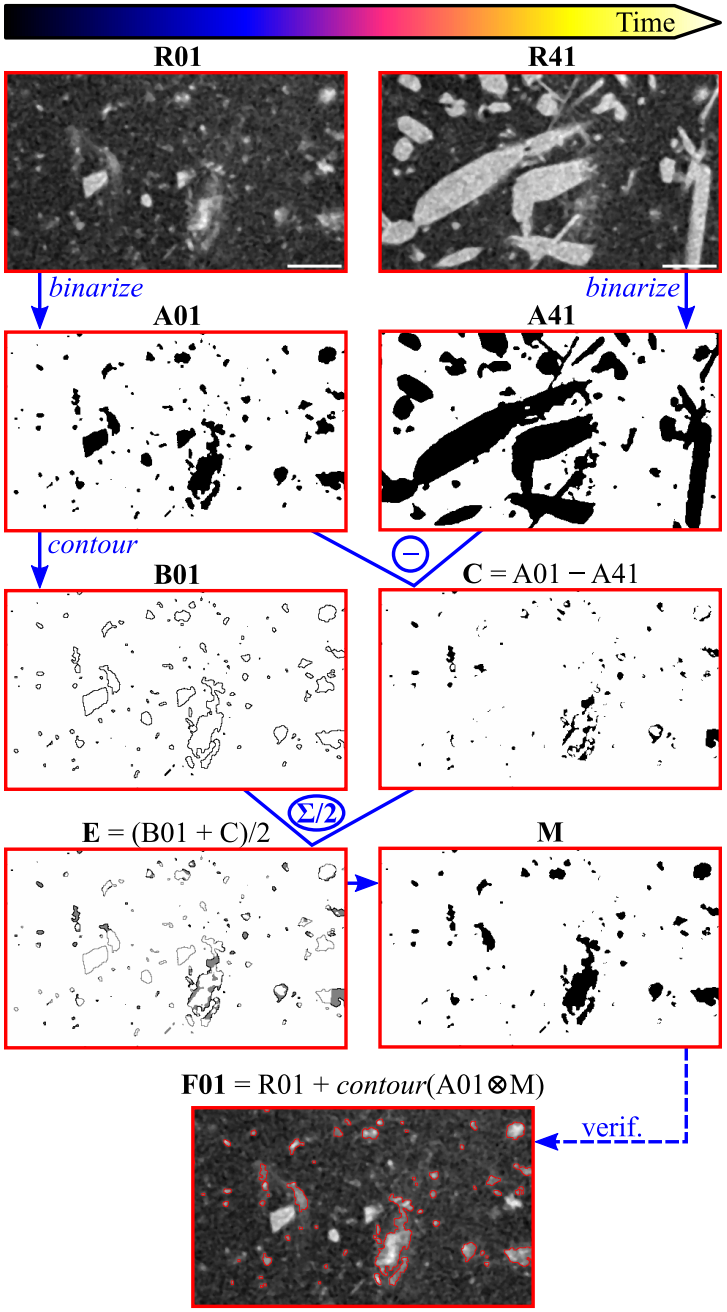

Figure S4: Illustration of the different steps to obtain a binary mask (denoted M) of HH particles from the raw image (denoted R) acquired at time t_1 (R01). R01 = 1st raw image of the experiment 1, collected at time t_1 (scale bar 10 µm). R41 = 41st raw image of the same region of interest (scale bar 10 µm). A01 = binary image obtained from R01 (time t_1). A41 = binary image obtained from R41. B01 = contours of the black particles in A01. C = A01 − A41. E = average of images B01 and C. M = HH binary mask at time t_1. F01 = overlay of the mask M on the raw image R01 to verify the quality of the mask M. Reproduced from doi: 10.6084/m9.figshare.23723673 © (2023) A. Fantou, CC BY 4.0 license https://creativecommons.org/licenses/by/4.0/.

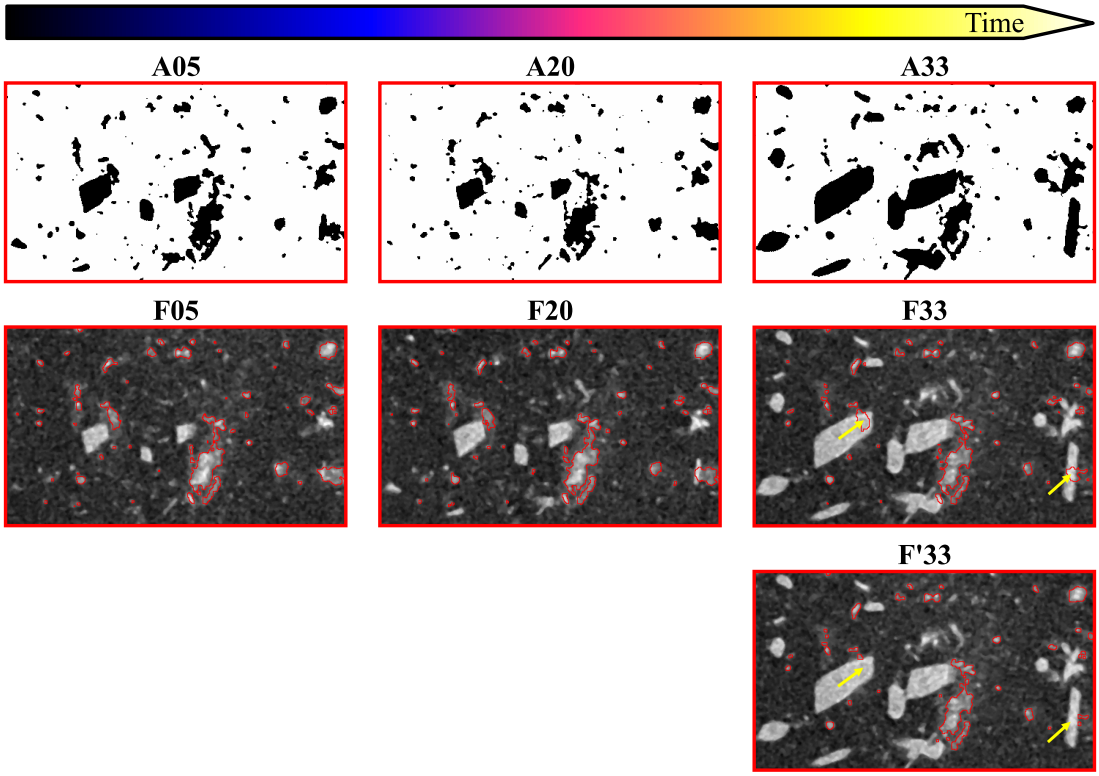

Figure S5: Illustration of the different steps to obtain a stack of binary images of HH particles. A05 = 5th binary image with all crystals in black. F05 = result (in red) of the AND operation between images M (see fig. S4 for a reminder on how were obtained the F images) and A5, overlaid to the 5th raw image (corresponding to R05). A20 = 20th binary image with all crystals in black. F20 = result (in red) of the AND operation between images M and A20, overlaid to the 20th raw image (corresponding to R20). A33 = 33rd binary image with all crystals in black. F33 = result (in red) of the AND operation between images M and A33, overlaid to the 33rd raw image (corresponding to R33). Yellow arrows show regions where DH crystals and HH mask overlap. F′33 = final mask of the HH particles obtained after subtraction from F33 of the regions where DH crystals and HH mask overlapped. No overlap is visible anymore, see yellow arrows. Reproduced from doi: 10.6084/m9.figshare.23723673 © (2023) A. Fantou, CC BY 4.0 license https://creativecommons.org/licenses/by/4.0/.

6.2. Evaluation of the detection depth using Monte Carlo simulations

Monte Carlo simulations using Hurricane software (from SAMx, Trappes, France) were performed to estimate below which depth DH crystals cannot be seen anymore in the Backscattered Electron images. To model the sample in the Quantomix cell, as no information was disclosed by the manufacturer, we assumed that the top membrane was 100 nm thick and made of a carbon-based polymer. The size of the computation box was set to 20 µm along each direction. The electron beam energy was set to 10 keV, as in the experiments, and 1 000 000 electron trajectories were computed. All electrons escaping the upper side of the computation box were considered as backscattered electrons. Different sample configurations were studied, with a dihydrate crystal immersed in water at different depths below the membrane (see table S1).

Table S1: Results obtained from Monte Carlo simulations performed on different computation boxes containing a dihydrate crystal immersed in water in a Quantomix cell. The thicknesses of water (W) and dihydrate (DH) are specificed in each case within brackets. F_i, F_w and F_d are the fractions of backscattered electrons for the configuration i, pure water (configuration #1) and pure dihydrate (configuration #2), respectively.

	Composition of the computation box					
Configuration number, i	1	2	3	4	5	6
Water (W)	20 µm	–	–	200 nm	400 nm	900 nm
Dihydrate (DH)	–	20 µm	500 nm	500 nm	500 nm	500 nm
Water (W)	–	–	19.5 µm	19.3 µm	19.1 µm	18.6 µm
Fraction of BSE, F [%]	9.28	15.31	15.35	13.04	10.86	9.26
Visibility of DH crystal, N [%]	0	100	100	62	26	0
Gray level	0	255	255	158	66	0

$N = (F_i - F_w)/(F_d - F_w)$

The fractions of backscattered electrons obtained from the simulations for each sample configuration are reported in the table S1 by the F parameter. When the cell is filled with water only (configuration #1, in table S1), 9.28% of the incident electrons are backscattered. This rate can be associated with regions in black (gray level set to 0) in the acquired images, as we wanted to maximize the contrast between water and crystals. When the cell is filled only with DH (configuration #2, in table S1), or contains a 500 nm thick layer of DH directly below the membrane (configuration #3, in table S1), the fraction of backscattered electrons reaches 15.3%. As this value is obtained for both configuration, we can conclude that the backscattered electrons come from the first 500 nm of dihydrate. We consider that it is the best detection of gypsum, and for both cases a gray level of 255 (*i.e.*, white) can be associated in the images.

In the case where the DH crystal is located far below the membrane, the fraction of backscattered electrons drops rapidly. It reaches the value found for water when the gypsum is 900 nm below the membrane. This means that gypsum is visible when it is located at 200 nm or 400 nm below the membrane, but it cannot be detected anymore at 900 nm. However, if we consider the gray level to be proportionnal to the visibility of DH crystal (N), the pixels with gypsum at a depth of 400 nm would have a gray level of 61. This is quite dark, and these pixels may not be considered as crystals. It seems more reasonable to consider that the DH crystals that are visible in the images come from a maximum depth of about 200 nm below the membrane, that is to say 300 nm from the top of the cell.